6-2014

Comparing Stellar Populations of Galaxies across the Hubble Sequence: Reduction of PISCES Near-Infrared Images

Vaishali Parkash
Union College - Schenectady, NY

Comparing Stellar Populations of Galaxies across the Hubble Sequence: Reduction of PISCES Near-Infrared Images

By

Vaishali Parkash

* * * * * * * * *

Submitted in partial fulfillment
of the requirements for
Honors in the Department of Physics and Astronomy

UNION COLLEGE
June, 2014

Acknowledgement

I would like to express my gratitude to the entire faculty and staff to the Union College Department of Physics and Astronomy, especially to Dr. Jon Marr for his moral support and help in planning my trips to Chile and advising me through writing process of my thesis. I also owe my deepest gratitude Dr. Catherine Kaleida and Dr. Nicole van der Bliek for offering me the opportunity to work on this research project at CTIO and helping me grow as a researcher for the past year. I would also like to thank Dr. Rolf Jansen, Shane Loeffler and the rest of CTIO REU/PIA 2014 students for their guidance and moral support throughout this thesis. Moreover, I would like to thank the Union College International Education Fund (IEF) and the Benjamin A. Gilman International Scholarship Program for the financial support that made it possible to travel to Chile to begin this research. Lastly, this work is dedicated to my parents, Ved and Varsha Parkash, who gave me unconditional love and support during my entire life and pushed me to follow my dreams.

Abstract

PARKASH, VAISHALI Comparing Stellar Populations of Galaxies across the Hubble Sequence: Reduction of PISCES Near-Infrared Images. Department of Physics and Astronomy, June 2014

ADVISOR: Catherine Kaleida (Cerro Tololo Inter-American Observatory), Rolf Jansen (Arizona State University) and Jonathan Marr (Union College)

To better understand the properties of high redshift galaxies and improve models of galaxy formation, we are investigating color radial profiles to study the stellar age, dust and metallicity distribution of galaxies of varying luminosities and morphological types. Current data obtained in the optical and UV have shown that early-type galaxies have a flat color profile, or are bluer at larger radii, while late-type spirals are redder with increasing radius. These trends are believed to be linked with stellar population ages or dust. To break the age-dust degeneracy as well as to avoid the metallicity dependence, we have obtained near-infrared images of Nearby Field Galaxy Survey (NFGS) galaxies taken with the PISCES Wide-field Infrared Camera on the 90-inch Bok Telescope. Combined with the optical and UV data, these new, near-infrared images will help better constrain these parameters and determine the ages of the stellar components of the galaxies. We discuss the method used to process and reduce the data and present the radial profile of the surface brightness and color of one particular galaxy in the sample, UGC 439.

Contents

1. Introduction

The study of galaxy morphology and classification is an ongoing task. The current model of galaxy classification originated with the Edwin Hubble classification system which he published in his book, *The Realm of the Nebulae* (Carroll & Ostlie 1996). His classification would later be known as the Hubble Sequence or Hubble Tuning Fork. According to Hubble, there were four types of galaxies: ellipticals (E's), lenticulars (S0), spirals (S's) and irregulars (Irr's). Elliptical galaxies, which make up the handle of the fork, are smooth elliptical objects. They are subclassified by how eccentric they are; E0 galaxies are very circular and E7 galaxies are the most elongated galaxies. The two prongs of the fork are made up of spiral galaxies. Spiral galaxies contain spiral-shaped arms that tighten into a bright central bulge. There are two types of spirals: barred spiral galaxies (SB) and normal spiral galaxies (S). They are also subclassified according to the tightness of their arms; Sa and SBa have the most tightly wound arms and large central bulges; Sc and SBc have the most loosely wound arms and small bulges. Lenticular galaxies, or S0 galaxies, are between the ellipticals and the spirals; they have a rotating disk with a bulge, but lack any spiral-like structure. If a galaxy did not have any of the above characteristics, it was classified as an irregular galaxy. Hubble also defined ellipticals as early type galaxies and spirals as late type galaxies (*The Hubble Tuning Fork* n.d.). It was thought that galaxies evolved from elliptical to spiral galaxies. It is now known that this is incorrect since elliptical galaxies rotate more slowly than spiral galaxies, therefore invalidating Hubble's theory of galaxy evolution.

Modern day updates have been made to the Hubble classification system including those used in the Third Reference Catalogue of Bright Galaxies by G. and A. de Vaucouleurs and their collaborators (Sparke & Gallagher 2000). They

eliminated irregular classes Irr I and Irr II and added spiral classes to the right of Sc or SBC. Their sequence of the normal late-type galaxies is given as S0, Sa, Sab, Sb, Sbc, Sc, Scd, Sdm, Sm, Im, Ir (Carroll & Ostlie 1996). Galaxies that are now considered Sd (SBd), Sm (SBm) or Im galaxies were originally part of the Irr I classes, where the m stands for Magellanic type. Galaxies in the Irr II are still considered to be irregular and are classified as IR galaxies (Carroll & Ostlie 1996).

To this day, models of galaxy formation are still being investigated. There are two basic models, the top-down and bottom-up or hierarchical model. The top-down model is similar to the solar system formation model in the sense that there was a dense cloud that began to collapse due to gravity, thus creating a protogalaxy. This model accurately predicts many of the characteristics of the Milky Way, such as the existence of the disk and why Population II stars, the older stars, are found in the halo and Population I stars are found in the disk (Carroll & Ostlie 1996). Some of the shortcomings of the top-down model are that it does not predict the retrograde orbits of halo stars that are observed or explain the wide range in ages or the compositional variation of globular clusters (Carroll & Ostlie 1996). The bottom-up model states that galaxies were formed from smaller clumps that merged together. This model can account for metal-rich central bulges and the characteristics observed of globular clusters(Carroll & Ostlie 1996).

The bottom-up model is currently favored over the top-down model because of observations of the early universe. In the past decades, deep field images, like the Hubble Deep Field (HDF) and the Hubble Ultra-Deep Field (HUDF) have provided a glimpse into the past (Williams et al. 1996; Beckwith et al. 2006). These images have provided us the tools to study the earliest stages of galaxy evolution to better our understanding of how present-day galaxies came to be. Many of these

highly-redshifted galaxies have physical properties similar to local irregular, peculiar, and merger galaxies, but are also more compact and less massive than similarly luminous nearby galaxies (Taylor et al. 2005). To gain a better insight in these high-redshift galaxies, we plan to study the characteristics of nearby, low luminosity, irregular, peculiar and merger galaxies.

Radial color profiles can provide information about the stellar populations, the metallicity and the dust distribution in a galaxy (Kaleida 2010; Taylor et al. 2005). They provide detailed insight into how the above characteristics vary between the inner and outer parts and between different morphological structures of a galaxy. Late-type spiral (Sd), irregular and merging galaxies were found to become redder with increasing radius (Taylor et al. 2005), while studies of the radial color profiles of nearby early-type field galaxies, including studies by Vader et al. (1988), Franx et al. (1989), Peletier et al. (1990), and Tamura & Ohta (2003), have shown that elliptical galaxies and early-type spiral galaxies (SO, Sa, Sb, and Sc) have a flat color gradient, or become slightly bluer with increasing radius. However, Vader et al. (1988) studied the color profiles of 35 early type galaxies, including 10 dwarf elliptical (dE) galaxies and found that dE galaxies become redder at larger radii. Jansen et al. (2000a) also discusses that galaxies brighter than $M_B = -17$ are found to be redder in the inner parts, while galaxies fainter than $M_B = -17$ are equally likely to be red or blue in the inner parts. These color profiles are thought to be due to the stellar population ages or the dust contained in the galaxy since no practical galaxy formation theory predicts a positive correlation between metal content and radius (Vader et al. 1988; Taylor et al. 2005; Kaleida 2010). Jansen (2000) found strong Hα emission in the bluer regions of galaxies, indicating the presence of current star-forming regions, which supports the premise that the color profile is due to the age of the stellar population.

Near-infrared (NIR) images can also provide insight into the stellar structures of galaxies by tracing the older stellar population. At red and longer wavelengths the less massive stars tend to dominate the light output of a galaxy, making it easier to study the older stellar population (Kaleida 2010). Many structures in a galaxy, like bars, rings and spiral arms, are gravitationally-induced. Since gravity is dependent on the mass of the system and the older less massive stars dominate the luminous mass of the galaxy, the structures of the galaxy are influenced by the older stellar population. Therefore to better understand these structures it would be productive to study the stellar distribution in a galaxy using NIR observations.

In particular, observations in J, H and K_s bandpasses can help us break the age-dust-metallicity degeneracy. A galaxy can become redder through multiple processes. A galaxy becomes redder as its stellar population becomes older and the young blue stars die out. Increase in metallicities can also redden the galaxy since the effective temperature of stars decreases with increasing opacities. The dust in a galaxy can also redden the color by absorbing the UV emission from young stars and remitting it in the IR. According to von Braun et al. (1998), the H-K color is insensitive to metallicity, but the J-K color is sensitive to the metal content. In addition, the J-K color provides a larger color measure because it spans a wider range in wavelength(Kaleida 2010).

In this paper we will describe the method used to process and reduce the PISCES data set and present surface photometry on UGC 439.

2. Sample Selection

The galaxies for this study were chosen from the 196-galaxy Nearby Field Galaxy Survey (NFGS) by Jansen (2000). The NFGS galaxies were chosen to provide a smaller sample of galaxies that are representative of nearby galaxies as a whole. The galaxies in the NFGS are a subsample of the 2400 galaxies in the Harvard-Smithsonian Center for Astrophysics Redshift Survey (CfA I) catalog (Huchra 1983). The CfA I catalog is nearly complete within its selection limits and contains galaxies that have been morphologically classified and with an absolute blue photographic magnitude (M_Z) from -22 to -13 for H_0= 100 km s^{-1} Mpc^{-1}.

Since the galaxy spectra for NFGS were obtained using the FAST spectrograph (Fabricant 1998) and the spectrograph had a slit size of about 3 arcmin, Jansen (2000) did not want to include galaxies that were larger than 3 arcmin. He also did not want to impose a strict diameter limit since it would introduce bias against low surface-brightness galaxies. Instead, Jansen imposed a lower limit on the radial velocity that increases with luminosity. Instead of comparing the size of each galaxy in the CfA I catalog to the slit size, he assumed that a galaxy with a certain radial velocity and luminosity would have a certain radius and by the Hubble Law, he assumed that galaxies with a radial velocity smaller than some limit are closer to the Earth and would appear larger than the slit size. The lower radial velocity limit was determined to be

$$V_{LGSR}(km/s^{-1}) > 10^{-0.19-0.2M_Z}, \tag{1}$$

where V_{LGSR} is the velocity taken with respect to the Local Group standard of rest and M_Z is the absolute blue photographic magnitude. The velocity with respect to

the Local Group standard of rest is defined as

$$V_{LGSR}(km/s^{-1}) = V_{helioSR} + 300\sin(b)\cos(l) \quad (2)$$

where $V_{helioSR}$ is the velocity relative to the Heliocentric standard of rest, b is the galactic latitude and l is the galactic longitude (Yahil et al. 1977). The NFGS also excludes galaxies in the direction of the Virgo Cluster in order to avoid a bias favoring a cluster population.

After these cuts, 1006 galaxies were left. To obtain a subsample that represents the full range in Hubble type and absolute magnitudes from the CfA1 galaxy survey, Jansen (2000) placed all the galaxies in one magnitude wide bins and then within each bin the galaxies were sorted by their Hubble types. Afterwards, for each bin he selected every Nth galaxy to get an even distribution of morphological types of the same magnitude. The value of N was the ratio between the total number of galaxies in a bin and desired number of galaxies from that bin (Marzke et al. 1994). Through this process, he created a list of 196 galaxies with a median redshift of 0.01 and a maximum redshift of 0.07. Since the NFGS contains a small number of galaxies but represents the wide range in Hubble type and absolute magnitude, it is a perfect survey for studying the color profile of galaxies.

Data available for the NFGS sample include U, B, and R surface photometry (Jansen et al. 2000a), nuclear and globally integrated spectra (Jansen et al. 2000b), and Two Micron All Sky Survey (2MASS) J, H, and K_s infrared images (Kirby et al. 2008). The 2MASS images of the NFGS sample are not sensitive enough for our study and the surface brightnesses produced do not extend beyond the central regions (Kirby et al. 2008). Therefore, we have obtained new NIR data of the NFGS sample in order to obtain a depth comparable to Jansen et al. (2000a).

Our goal for this study is to obtain NIR data for many galaxies in the NFGS. We are currently in the process of observing and obtaining more data. The galaxies of which we have already obtained data were chosen based on a priority list and which were visible at the time of the year that the data were taken.

3. Observational Methods

3.1. Observations

In this thesis, we processed NIR images of 11 galaxies, obtained previously by Jansen and Kaleida using the PISCES Wide-field Infrared Camera on the 90-inch Bok Telescope. We analyzed and produced radial profiles of one galaxy so far to determine the contribution of the stellar population, dust, and metal content to the color gradients, and to trace the older stellar populations for a range of nearby galaxies. The low-sensitivity data from the 2MASS survey do not constrain well the extinction by the interstellar dust and the stellar masses in these galaxies. With the deeper images in J, H and K_s from the PISCES instrument, we aim to put tighter constraints on these parameters. The PISCES instrument with the 90-inch Bok Telescope was well suited for this project. The 8.5 x 8.5 arcmin field of view at f/9 provides us with deep and wide-field near-infrared images that can be used to study the extinction by interstellar dust and the stellar masses of these galaxies in combination with the UV and optical data available.

The PISCES instrument is a 1024x1024 pixel HgCdTe camera designed by McCarthy et al. (2001). It provides a plate scale of 0.5 arcsec /pixel when used on the 90-inch Bok Telescope. It has a system gain of about $4.55 \pm 0.04\ e^-/ADU$ and a read noise of $5.13 \pm 0.04\ ADU$ (McCarthy et al. 2001).

The observations were taken on 2010 October 28-31. For completeness, Table 1 lists all the galaxies observed during this run, general characteristics and information about the observations. This paper though, only presents the results of UGC 439. Column (1) lists the galaxies names. Columns (2) and (3) list their equatorial coordinates that were measured from the Digital Sky Survey. Column (4) lists the velocities with respect to the Local Group standard of rest. Column (5) lists their distances, which was derived from the velocities from column (4) assuming H_0=73 km s^{-1} Mpc^{-1}. Column (6) lists the morphological types according to the Hubble sequence. Column (7) lists the ellipticity of the galaxy. Columns (8-10) list the filters, the number of non-photometric and photometric images. Non-photometric images are used as additional exposures to attain the sensitivity needed to study the outer regions of the galaxy, while only photometric images are used to obtain the calibration solutions. Further detail is provided in Section 3.3.

Each galaxy was observed with J, H, and K_s filters (1.275, 1.63 and 2.12 μm, respectively) and in four dither positions, where the galaxy was imaged in each quadrant in order to account for bad pixels. Multiple exposures with small dithers were taken at each large dither position. Images of seven standard stars were also obtained. The observing conditions of October 31 were photometric and therefore several Persson et al. (1998) standard stars were observed at low and high air masses for photometric calibration.

Table 1. Observed NFGS Galaxy List

Object	RA[a] (h m s)	Dec[a] (° ′ ″)	V_{LG}[b] (km/s)	Distance[c] (Mpc)	Type[a]	Ellipticity[a]	Filter	# of Non-photometric Images	# of Photometric Images
(1)	(2)	(3)	(4)	(5)	(6)	(7)	(8)	(9)	(10)
NGC 7194	22 03 30.9	+12 38 12	8300 ± 17	113.7 ± 8.0	E	0.3077	J	37	4
							H	65	4
							K_s	65	4
IC 1776	02 05 15.2	06 06 25	3521 ± 8	48.2 ± 3.4	Sc	0.0435	J	50	4
							H	65	4
							K_s	65	4
UGC 2704	03 22 47.4	-01 55 22	8236 ± 27	112.8 ± 7.9	Sa	0.0	J	41	4
							H	33	4
							K_s	46	4
UGC 439	00 41 21.5	-01 42 57	5441 ± 10	74.5 ± 5.2	Sa	0.0	J	20	4
							H	20	4
							K_s	20	4
UGC 12856	23 56 45.2	+16 48 50	2011 ± 14	27.5 ± 1.9	Im	0.6538	J	30	20
							H	33	28
							K_s	32	28
NGC 1552	04 20 17.7	-00 41 34	4745 ± 8	65 ± 4.6	S0	0.25	J	10	92
							H	13	52
							K_s	13	52
NGC 7460	23 01 42.9	+02 15 49	3401 ± 14	46.6 ± 3.3	Sb	0.090	J	0	12
							H	0	52
							K_s	0	12
UGC 313	00 31 26.1	+06 12 24	2267 ± 11	31.1 ± 2.2	Sd	0.4286	J	0	4
							H	0	4

Table 1—Continued

Object	RA[a] (h m s)	Dec[a] (° ′ ″)	V_{LG}[b] (km/s)	Distance[c] (Mpc)	Type[a]	Ellipticity[a]	Filter	# of Non-photometric Images	# of Photometric Images
(1)	(2)	(3)	(4)	(5)	(6)	(7)	(8)	(9)	(10)
							K_s	0	4
IC 195	02 03 44.6	+14 42 33	3792 ± 9	52 ± 3.6	S0/a	0.4667	J	0	14
							H	0	11
							K_s	0	11
NGC 2780	09 12 44.4	+34 55 32	1939 ± 9	26.6 ± 1.9	Sab	0.3	J	0	4
							H	0	4
							K_s	0	4
NGC 2799	09 17 31.0	+41 59 39	1671 ± 4	22.9 ± 1.6	Sm	0.7619	J	0	4
							H	0	4
							K_s	0	4

[a]Retrieved from Jansen et al. (2000a).

[b]Retrieved from Karachentsev & Macharov (1996).

[c]Retrieved from NASA/IPAC Extragalactic Database.

3.2. Reduction

The data were reduced within the IRAF environment. The steps of the reduction pipeline were: (1) correct for crosstalk, (2) combine dark frames, (3) subtract dark current, (4) create flat frame using either science frames or standard star frames, (5) correct for pixel variation using flat frames, (6) sky subtraction, (7) apply a bad pixel mask, (8) align images, (9) stack the images, and (10) flatten the background. The following subsections will provide further information of these processes.

3.2.1. Crosstalk Correction

The first step in the pipeline was to correct for crosstalk using a program called *corquad*. Crosstalk between the quadrants causes each pixel in one quadrant to leave an "echo", or a negative imprint of about 0.1%, and a tail in the other quadrants. *Corquad* can successfully remove the ghost of faint stars, but it leaves minor ghosts due to saturated stars, which is not a problem for our purposes.

3.2.2. Correction of Dark Current

The next step was to correct for dark current. Even when the detector is not exposed to light, a signal, or dark current, is still generated due to the temperature of the detector. In order to eliminate the dark current, dark frames, which are taken with the shutter closed of the same exposure time, are subtracted from the science frames.

The number of dark frames and their exposure times varied from night to night during the run. The dark calibration frames were created by using a median filter of stacks of dark frames of the same exposure time and night. Also, darks from the

beginning of the night were combined apart from the dark frames taken at the end of the night since the darks taken at the beginning of the night show some structure that may be due to a transient effect of the detector reaching a stable temperature after the liquid nitrogen coolant was refilled.

Once the combined dark frames were created, the appropriate dark calibration frames were subtracted from the science and the standard star frames. For a third of the images of UGC 439, we did not have dark frames of the appropriate exposure time during a particular night. In consideration of scaling the existing dark frames to the needed exposure times we tested the linearity of the response of the detector. For a visible CCDs, we would expect the dark count should increase with time, but infrared detectors are created using different materials and have a different quantum behavior than CCDs. In Fig.1, we have plotted the relationship between the mean count level of a dark and its exposure time. Each color represents a different night

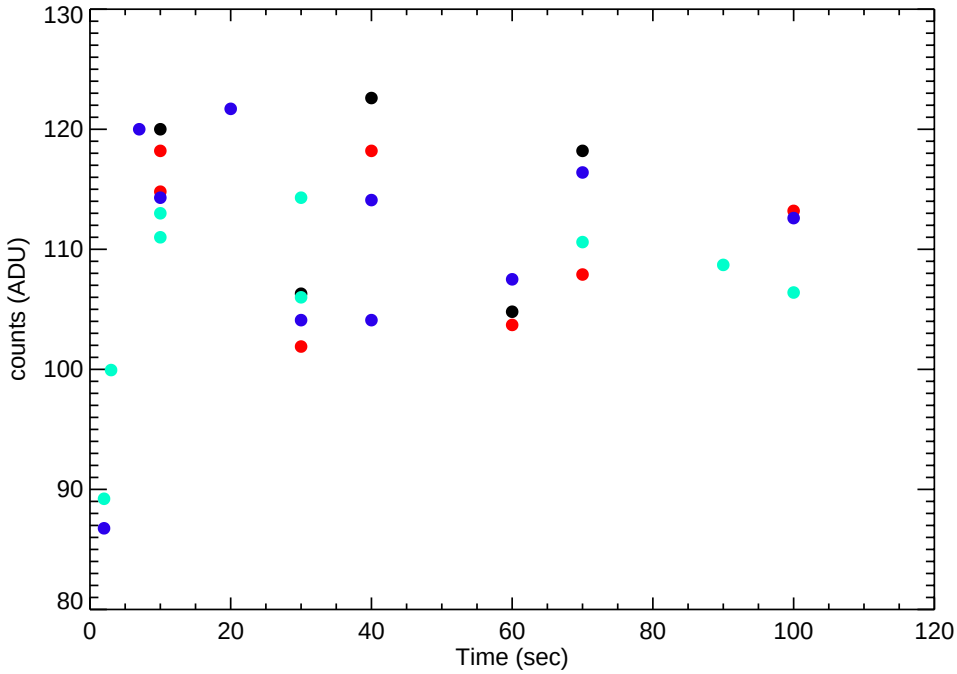

Fig. 1.— Mean count level versus exposure time of dark frames. Each color represents a different night during the run.

during the run. As shown, there is no apparent relationship between the count level and the exposure time. Since the detector is not linear, we were not able to interpolate the dark frames for those exposure times. Therefore, the median was taken of all the darks of the same exposure time, but not dependent on the night. This new median was subtracted from the science frames that did not have dark frames of the appropriate exposure time.

3.2.3. Flat Frames and Sky Subtraction

Pixels on the detector do not have the same quantum efficiency. Also, the detector may also have features such as a gradient due to non-uniform illumination and a cross mark due to separation of the quadrants. These features can be corrected by dividing the science frame by a flat frame.

Flat field frames were created using either dithered science frames or standard star frames that were dark-current corrected. In order to create flat fields using science frames, the images needed to be well dithered; there cannot be repeating frames where the galaxy occupies the same region on the detector. Standard star frames that did not have a crowded field were also used. These frames were average combined and normalized to create one flat field per filter per day.

An average of 10 frames were used to create each flat field frame. It should be noted that McCarthy et al. (2001) states that J and H flat fields can be created using science frames, but this method does not work as well when creating a K_s flat field since K_s is sensitive to the thermal background from the night sky. McCarthy et al. (2001) recommend taking a sky flat right after sunset and also creating a flat frame from science frames, and then subtracting the two frames in order to remove the thermal component and create a proper K_s-band flat field.

Afterwards, all the dark-subtracted science frames were divided by the appropriate flat field. Then the science frames were rotated $-90°$ and reflected across the x-axis so the orientation matched the sky. A sky frame was subtracted in order to remove the thermal noise of the background sky and a bad pixel mask was applied.

Fig.2 shows a J-band science frame of NGC 439 after several steps in the processing. The galaxy is encased in a circle with a radius of 70 pixels (35″). We show images after: (1) crosstalk correction, (2) dark current correction, (3) flat fielding and (4) sky subtraction.

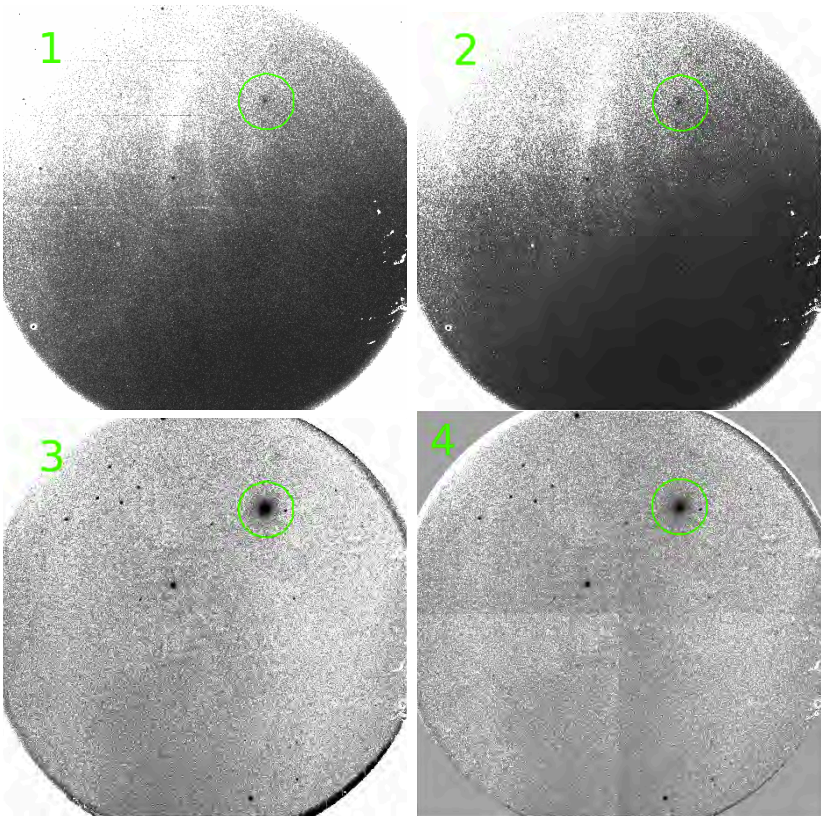

Fig. 2.— J-band science frame of NGC 439 after each step in the processing. The galaxy is encased in a circle with a radius of 70 pixels (35 arcsec). The frames show images after (1) crosstalk correction, (2) dark current correction, (3) flat fielding and (4) sky subtraction.

3.2.4. Alignment and Stacking

Before aligning the images, we first corrected for pin-cushion distortion demonstrated in Fig. 3. The pin-cushion distortion increases the plate scale with distance from the center of the image. We first obtained a $17' \times 17'$ 2MASS J-band mosaic image centered on each galaxy which closely matched the pixel scale of the PISCES using the on-line 'Montage' service at IRSA/IPAC. Then, by using the IRAF task *imregister*, the science frames were aligned to the 2MASS image and corrected for distortion by treating the image as if it were a rubber sheet, shifting, rotating and compressing or stretching the image until the stars in the image match up with the stars in the 2MASS image.

Before stacking the images, the exposure times were each normalized to one second.

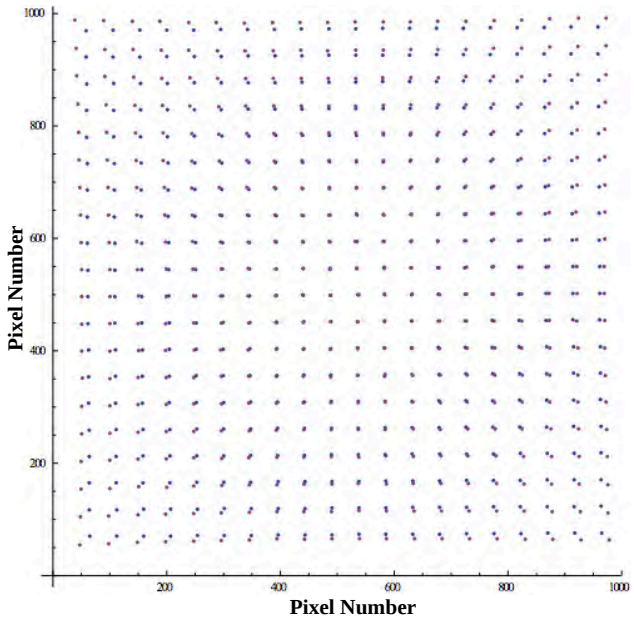

Fig. 3.— Sample plot of the pin-cushion distortion of PISCES. The raw points (red) and the corrected points (blue) show pin-cushion distortion with peak value of about 20 pixels (Guerra et al. 2013).

Since the images were taken at different airmasses during the non-photometric and photometric nights, the counts of non-photometric images were scaled to the counts of the photometric images. This scale factor was determined for each independent non-photometric image. Aperture photometry was performed on the galaxy of interest in each image to determine the flux count. Then the average count of the galaxy in the photometric images was divided by the count of the galaxy image in a non-photometric night to determine the scale factor. Then each pixel in an image was multiplied by its scale factor. As a result, when subtracting the non-photometric scaled image from a photometric image, the galaxy is subtracted out. Theoretically, scaling the non-photometric images will allow us to apply the photometric solutions of the photometric images (Jansen et al. 2000a). In the stacked image, non-photometric images help us gain more depth, while the photometric images provide the photometric solutions. The images were stacked weighted according to the inverse of their standard deviation. The standard deviation of each image was calculated in different patches in the sky of each image and the average was taken. Twenty-three frames were stacked to create the final J and H images and twenty-two were stacked to create the final K_s image.

The final step in the pipeline was to flatten the sky background in order to correct for the gradient in the sky and the "seams" in the checker-board pattern, which are due to the separation of the quadrants. Fig.4 compares a sky flattened stacked image to 2MASS images of UGC 439 in each band. The 1^{st} row shows the images in the J-band, the 2^{nd} row shows the H-band, and the 3^{rd} row shows the K_s-band.

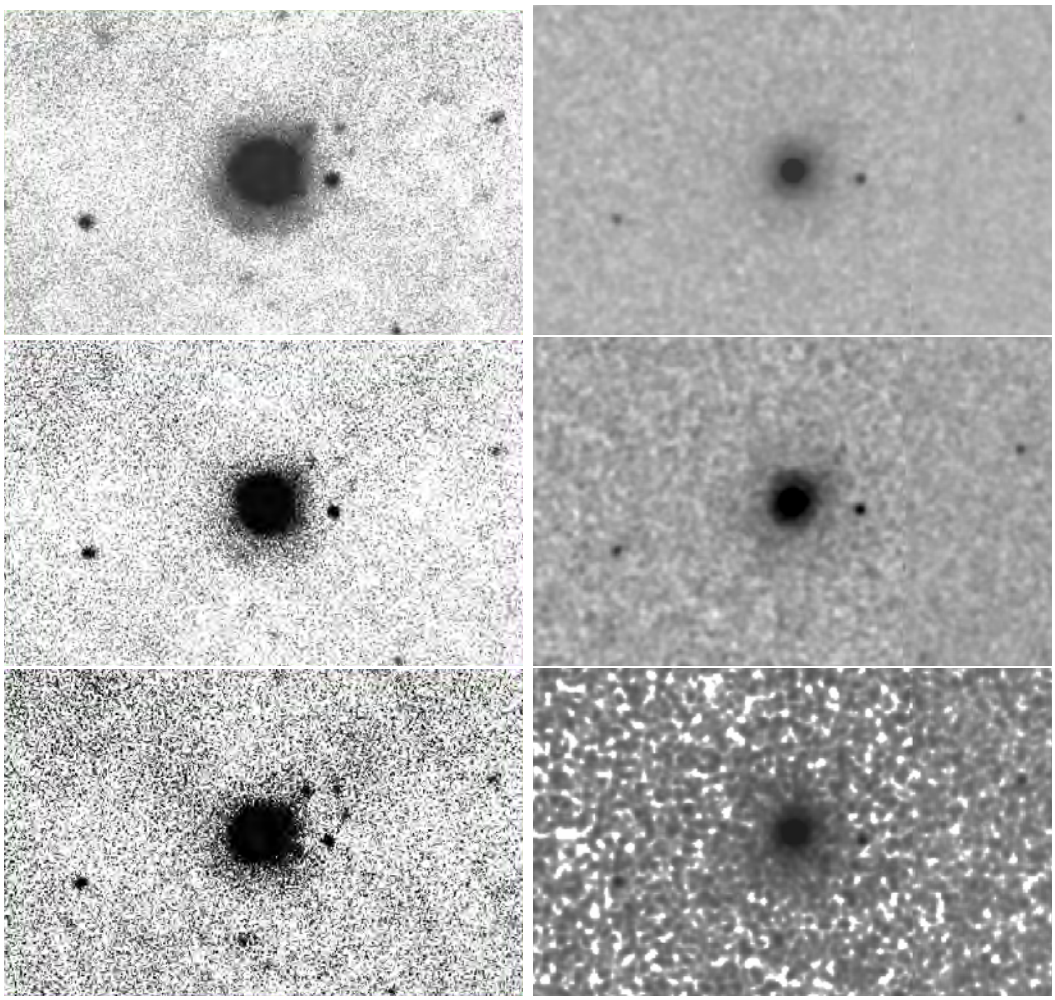

Fig. 4.— Left to Right: The final processed science frame, and the 2MASS image. Top to Bottom: J-band, H-band and K_s-band.

3.3. Calibration

In order to determine the photometric calibration of our run, we measured the instrumental magnitudes of multiple Persson et al. (1998) standard stars observed on the photometric night. We used initial aperture radii of 2, 4, 6, 8,10 and 12 pixels corresponding to 1", 2", 3", 4", 5", and 6" respectively. Then by fitting a curve of growth to the results of the aperture photometry, we determined the aperture corrections for each star and airmass and extrapolated their aperture magnitudes. Table 2 presents a list of standard stars. Column (1) lists the name, columns (2-3) list the filter and the airmass at which they were observed, and columns (4-6) list the aperture correction, the instrumental magnitudes and the best aperture radius.

Table 2. Standard Stars

Object	Filter	Airmass	Aperture Correction (mag)	Instrumental Magnitudes (mag)	Aperture radius (pixels)
(1)	(2)	(3)	(4)	(5)	(6)
P161-D	J	1.05	-0.51 ± 0.04	-9.981 ± 0.003	10
		1.2425	-0.70 ± 0.05	-9.957 ± 0.001	6
	H	1.05	-0.49 ± 0.04	-10.038 ± 0.002	12
		1.255	-0.064 ± 0.004	-10.066 ± 0.003	12
	K_s	1.05	-0.48 ± 0.03	-9.611 ± 0.006	8
		1.2675	-0.63 ± 0.05	-9.599 ± 0.005	10
P530-D	J	1.1525	-0.74 ± 0.05	-10.348 ± 0.051	10
		1.1725	-0.71 ± 0.05	-10.099 ± 0.001	6
	H	1.16	-0.92 ± 0.07	-10.499 ± 0.002	16
		1.185	-1.05 ± 0.08	-10.470 ± 0.003	8
	K_s	1.1675	-0.66 ± 0.05	-10.059 ± 0.005	10
		1.195	$-.071 \pm 0.05$	-10.037 ± 0.004	12
S889-E	J	1.21	-1.02 ± 0.07	-9.642 ± 0.004	10
		1.5775	-0.80 ± 0.06	-9.584 ± 0.006	10
	H	1.22	-0.99 ± 0.07	-9.814 ± 0.003	12
		1.605	-0.77 ± 0.06	-9.799 ± 0.004	12
	K_s	1.225	-0.89 ± 0.06	-9.346 ± 0.006	8
		1.6375	-0.68 ± 0.05	-9.313 ± 0.006	10
P525-E	J	1.715	-0.84 ± 0.06	-9.963 ± 0.003	14
	H	1.6775	-0.89 ± 0.07	-10.159 ± 0.004	12
	K_s	1.6425	-0.65 ± 0.05	-9.559 ± 0.005	6
S840-F	J	1.345	-0.57 ± 0.04	-10.197 ± 0.002	12
	H	1.3325	-0.82 ± 0.06	-10.322 ± 0.003	10
	K_s	1.33225	-0.46 ± 0.03	-9.875 ± 0.004	10

For each filter, we used an IRAF interactive fitting procedure *mkimsets* in determining the zero point, Z_λ, extinction value, ϵ_λ, and color term, c_λ. Eq. 3 summarizes the fits that were applied to extract the photometric calibrations:

$$\begin{cases} J = J_i - Z_J - \epsilon_J X - c_J(J - K_s), \\ H = H_i - Z_H - \epsilon_H X - c_H(H - K_s), \\ K_s = K_{s,i} - Z_{K_s} - \epsilon_{K_s} X - c_{K_s}(J - K_s), \end{cases} \tag{3}$$

where J_i, H_i and $K_{s,i}$ are the instrumental magnitudes and X is the average airmass of the image. We paired J with K_s for both the J and K_s calibration equations instead of pairing J with H, or K_s with H because for each equation, J paired with K_s produced a better fit.

We found a discrepancy between our zero points and extinction values, as summarized in Table 3, and the published values (Guerra et al. 2013). We adopted the photometric calibration values that we determined, since the residuals of the calibration fits (Eq. 3) showed an rms of 0.007, 0.001 and 0.01 for a range of instrumental magnitude in the J, H, and K_s bands respectively, as shown in Fig.5. Appendix B discusses another method to determine the photometric calibrations that we considered, but we decided against it due to large errors in the fit.

Using a similar procedure described in Jansen et al. (2000a), we photometrically calibrated the radial intensity profiles by simultaneously solving for the calibration

Table 3. Photometric Constants

Filter	Z	σ_Z	ϵ	σ_ϵ	c	σ_c
J	-21.78	0.01	0.115	0.008	-0.002	0.005
H	-21.518	0.005	0.036	0.003	0.001	0.008
K	-21.15	0.02	0.155	0.009	0.001	0.003

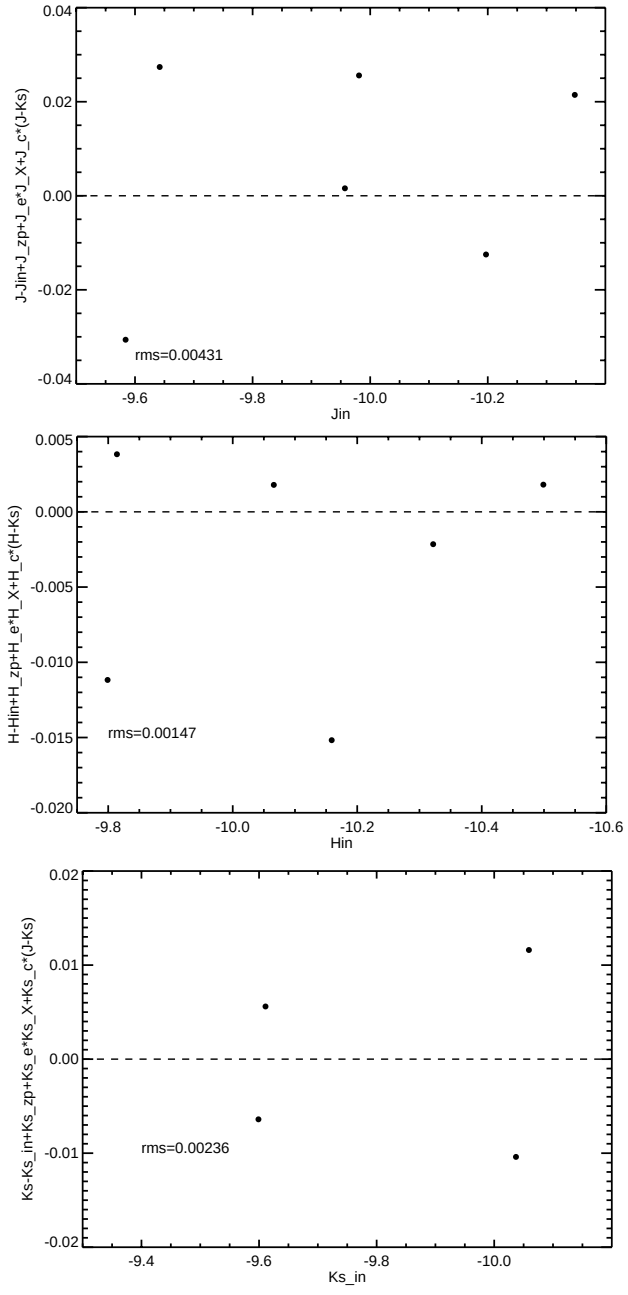

Fig. 5.— From top to bottom: The residuals of the J-band calibration fit versus the J instrumental magnitudes, the residuals of the H-band calibration fit versus the H instrumental magnitudes, and residuals of the K_s-band calibration fit versus K_s instrumental magnitudes. Theoretically, the data should lie on the line y=0 since the y-axis plots the residuals of each fit.

equations for J, H and K_s. Similar to Equations 3, Equations 4 summarize the calibration equations for J, H and K_s intensity profiles:

$$\begin{cases} \mu_J(r) = \mu_{J,i}(r) - Z_J - \epsilon_J X - c_J(\mu_J - \mu_{K_s})(r), \\ \mu_H(r) = \mu_{H,i}(r) - Z_H - \epsilon_H X - c_H(\mu_H - \mu_{K_s})(r), \\ \mu_{K_s}(r) = \mu_{K_s,i}(r) - Z_{K_s} - \epsilon_{K_s} X - c_{K_s}(\mu_J - \mu_{K_s})(r), \end{cases} \tag{4}$$

where $\mu_{\lambda,i}$ denotes the surface brightness in instrumental magnitude per square arcsec. By defining $P_\lambda(r)$ as $\mu_{\lambda,i}(r) - Z_\lambda - \epsilon_\lambda X$, we can rewrite Equations 4 as:

$$\begin{cases} (1 + c_J)\mu_J(r) = P_J(r) + c_J\mu_{K_s}(r), \\ (1 + c_H)\mu_H(r) = P_H(r) + c_H\mu_{K_s}(r), \\ (1 - c_{K_s})\mu_{K_s}(r) = P_{K_s}(r) - c_{K_s}\mu_J(r). \end{cases} \tag{5}$$

Then by substituting each equation into each other, we find that the solutions for the surface brightnesses are:

$$\mu_J(r) = \frac{P_J(r)(1 - c_{Ks}) + c_J P_{Ks}(r)}{1 + c_J - c_{K_s}},$$

$$\mu_{K_s}(r) = \frac{P_{K_s}(r)(1 + c_J) - c_{K_s} P_J(r)}{1 + c_J - c_{K_s}} \tag{6}$$

and

$$\mu_H(r) = \frac{P_H(r)(1 + c_J - c_{K_s}) + c_H(P_{K_s}(r)(1 + c_J) - c_{K_s} P_J(r))}{1 + c_J + c_H - c_{K_s} + c_J c_H - c_H c_{K_s}}.$$

Assuming that the individual errors, $\sigma_{\mu_\lambda}(r)$, in the color terms are Gaussian in nature and uncorrelated, the random errors of the surface brightnesses are:

$$\begin{cases} \sigma_{\mu_J}(r) = \dfrac{1}{nm}\sqrt{(1-c_{K_s})^2\sigma^2_{P_J} + c^2_J\sigma^2_{P_{K_s}} + [\mu^2_J(r)+P^2_J]\sigma^2_{c_{K_s}} + [\mu^2_J(r)+P^2_{K_s}]\sigma^2_{c_J}} \\ \\ \sigma_{\mu_{Ks}}(r) = \dfrac{1}{nm}\sqrt{(1+c_J)^2\sigma^2_{P_{K_s}} + c^2_{K_s}\sigma^2_{P_J} + [\mu^2_{K_s}(r)+P^2_J]\sigma^2_{c_{K_s}} + [\mu^2_{K_s}(r)+P^2_{K_s}]\sigma^2_{c_J}} \\ \\ \sigma_{\mu_H} = \dfrac{1}{nm(1+c_H)}\sqrt{((1+c_J)c_H)^2\sigma^2_{P_{K_s}} + c^2_H c^2_{K_s}\sigma^2_{P_J} + nm^2\sigma^2_{P_H} + [\mu^2_H(r)+P^2_H]\sigma^2_{c_{K_s}}} \\ \qquad\qquad \overline{+[\mu^2_H(r)+P^2_H]\sigma^2_{c_J} + [\mu^2_H(r)+P^2_{K_s}]\sigma^2_{c_H}}, \end{cases} \tag{7}$$

where $nm = 1 + c_J - c_{K_s}$.

The radial surface brightness profiles are also corrected for Galactic extinction as given by Schlafly & Finbeiner (2011). These corrections in J, H, and K_s are 0.016, 0.010 and 0.007 magnitudes, respectively.

3.4. Photometry

In order to perform aperture photometry of UGC 439, circular annuli were fitted to the galaxy. The width of the fitted circular annuli grew by a factor of 1.1 to maintain a nearly constant signal-to-noise ratio to compensate for the decline in surface brightness with radius. The light was measured in annuli from 0.1951" to 62.3". Fig.6 displays the J-band stacked image of UGC 439 showing the outermost annulus edge in red and the inner and outer radii of the sky annulus in blue.

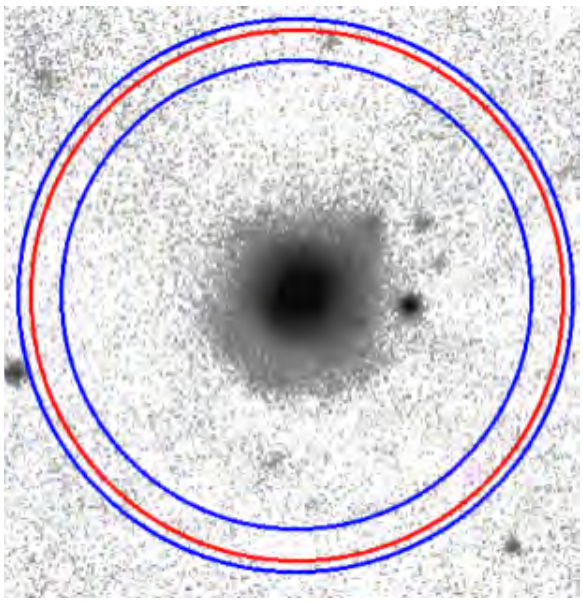

Fig. 6.— The final J-band image of UGC 439. The red circle represents the outer most annulus boundary at a radius of 124.6 pixels (62.3") from the center of the galaxy. The blue circles represents the inner and outer radii of the sky annulus at a radius of 110 to 130 pixels (55" to 65").

4. Results

In Fig. 7 we present the infrared surface brightness and color radial profiles of UGC 439. The colors seem to become redder with radius, but within the errors, the color profile may be flat. Fig. 8 presents the R band image, the U, B and R surface brightness radial profiles and B-R and U-B color radial profiles for UGC 439 reported by Jansen et al. (2000a). As expected for an Sa galaxy, the color profiles of UGC 439 are flat in the visible and infrared wavelength regime. The visible data of Jansen et al. (2000a) have much smaller errors than our infrared data because the noise in the infrared is much greater than in the visible. We overlapped both wavelength regimes in Fig. 9. The infrared surface brightness decreases as a function of radius just as the visible surface brightness does.

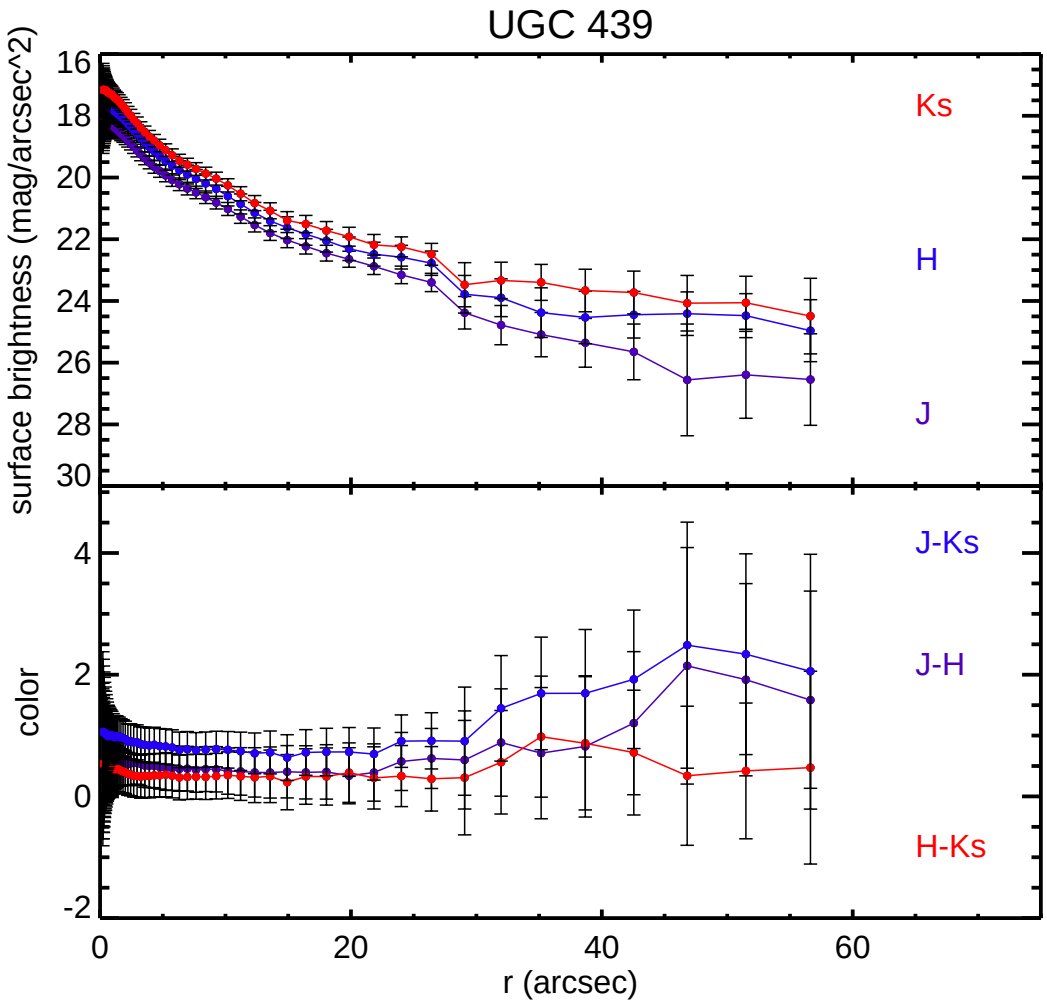

Fig. 7.— The radial dependence of the surface brightness in J, H and K_s(top panel) and corresponding colors (bottom panel) are presented for UGC 439.

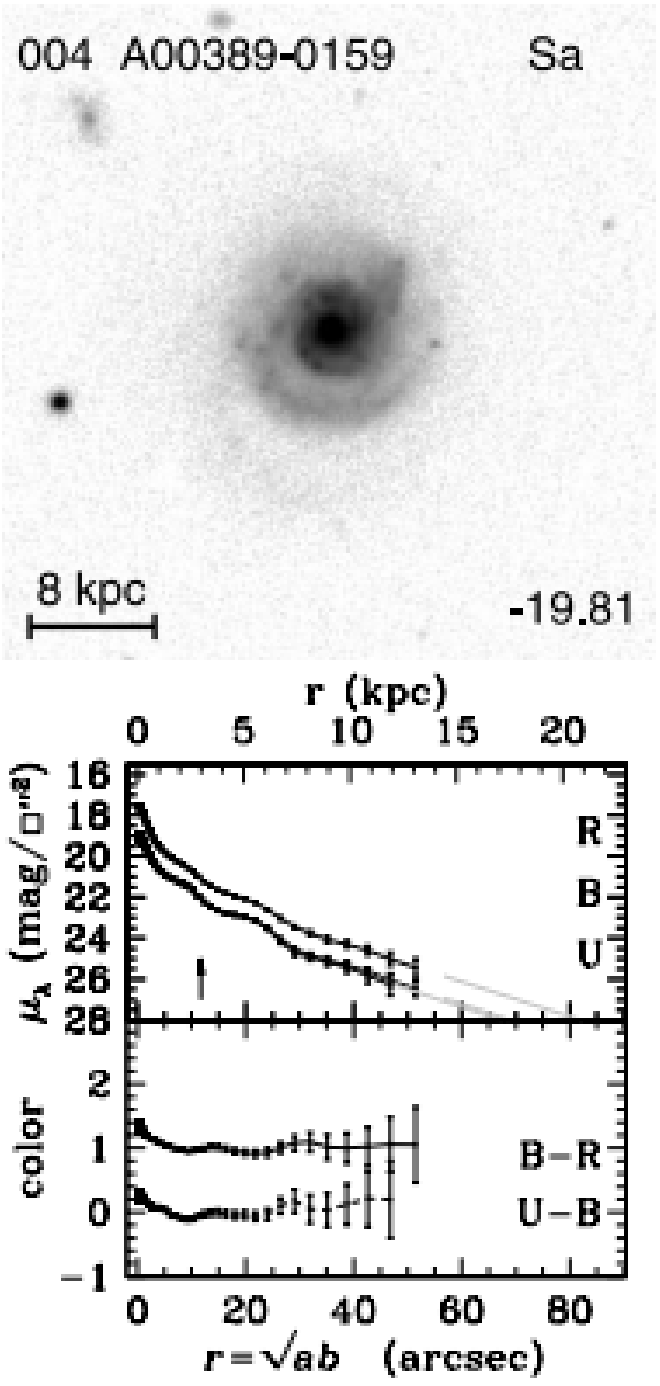

Fig. 8.— The R band image and the radial profiles of UGC 439. The radial dependence of the surface brightness in U, B and R (top panel) and corresponding colors (bottom panel) (Jansen et al. 2000a).

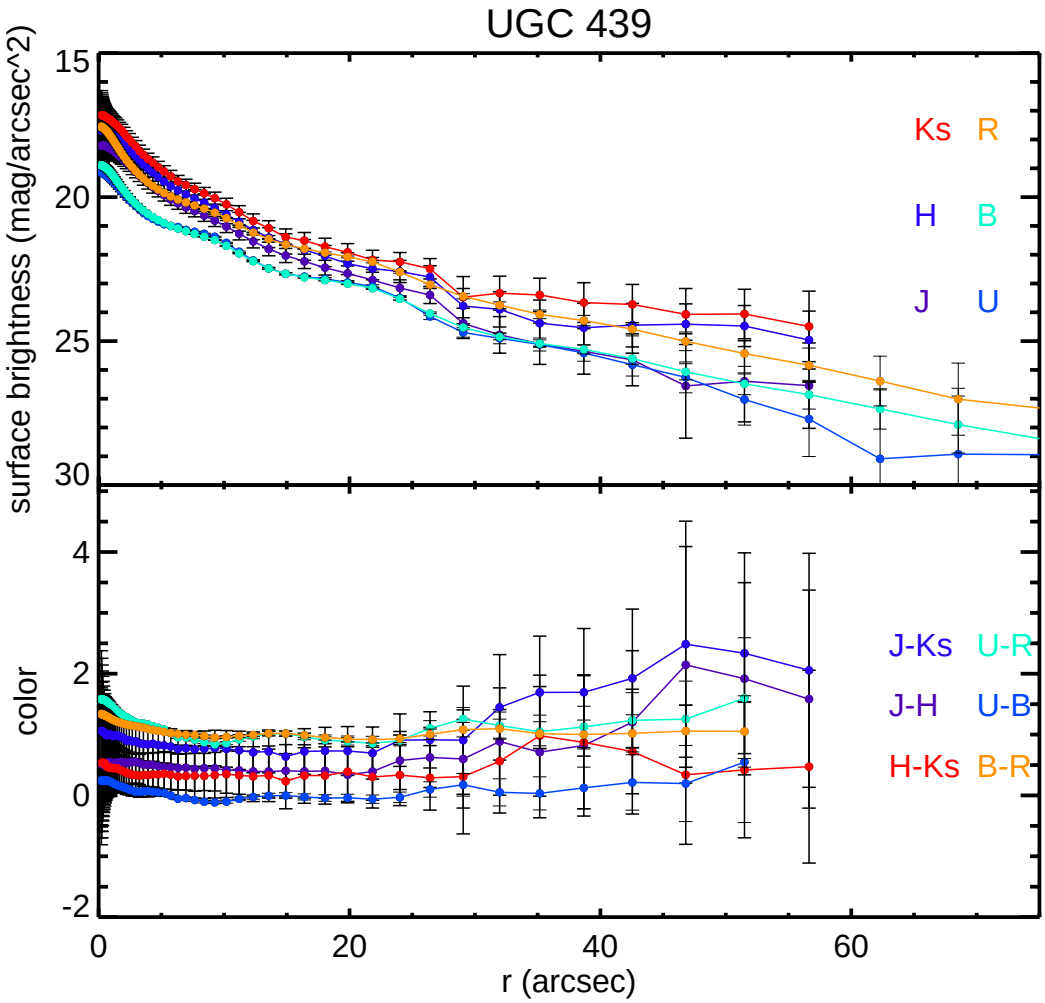

Fig. 9.— The radial dependence of the surface brightness in J, H and K_s overlapped with R, B, and U surface brightness from Jansen et al. (2000a)(top panel) and corresponding colors (bottom panel) are presented for UGC 439.

5. Discussion

In order to determine the stellar age and the dust component of UGC 439, we plan to combine the already available UV and visible data with our infrared data to create and fit a spectral energy distribution (SED). An SED can separate the stellar and dust components of the color radial profiles and help us determine which component affects the color profile of the galaxy the most.

We also plan to extract radial profiles from the other 11 galaxies in the PISCES data set. Since these galaxies have a non-zero ellipticity, we need to develop code for performing aperture photometry with elliptical annuli. Once we extract radial profiles of these other 11 galaxies, we will also fit an SED to each galaxy.

5.1. Infrared Side Port Imager (ISPI)

We also plan to expand our data set and take observations of more NFGS galaxies in the NIR. Since the PISCES instrument has been decommissioned, we have proposed for observing time using Infrared Sideport Imager (ISPI) on the 4 meter Blanco Telescope on Cerro Tololo. ISPI is a 2048x2048 pixel array detector with 0.303 arcsec/pixel resolution and a 10.25x10.25 arcmin field of view.

We have received one night of observing during April 2014 and half a night during the a re-commissioning night in late 2013. Shane Loeffler from the University of Minnesota, Duluth was able to to fully process the images of IC 1639 taken on the re-commissioning night during CTIO REU program. Fig 10 presents the R band image and radial profiles of the U, B and R bands (Jansen et al. 2000a) and Fig. 5.1 presents the ISPI J band image processed by Loeffler and the radial profiles of the J, H and K_s bands of IC 1639. In Fig. 12 we show the profile in the two wavelength regimes. Photometric calibrations for ISPI were determined using the

2MASS stars in the images as described in Appendix B. The radial profiles were extracted using the code developed in this thesis and aperture photometry was performed using circular annuli. To obtain a more accurate radial profiles, elliptical annuli will be used in the future. The infrared color profiles closely correspond with the optical profile and are flat as a function of radius. The surface brightness in both wavelength regimes drop smoothly as expected from an elliptical galaxy due to their homogeneous stellar population. Comparing the error in the infrared colors to the optical colors, we have concluded that the current dataset of ISPI data are not sufficient to study IC 1639 at radii as large as Jansen et al. (2000a). As we obtain more observing nights and data, we will greatly increase the depth of our infrared images.

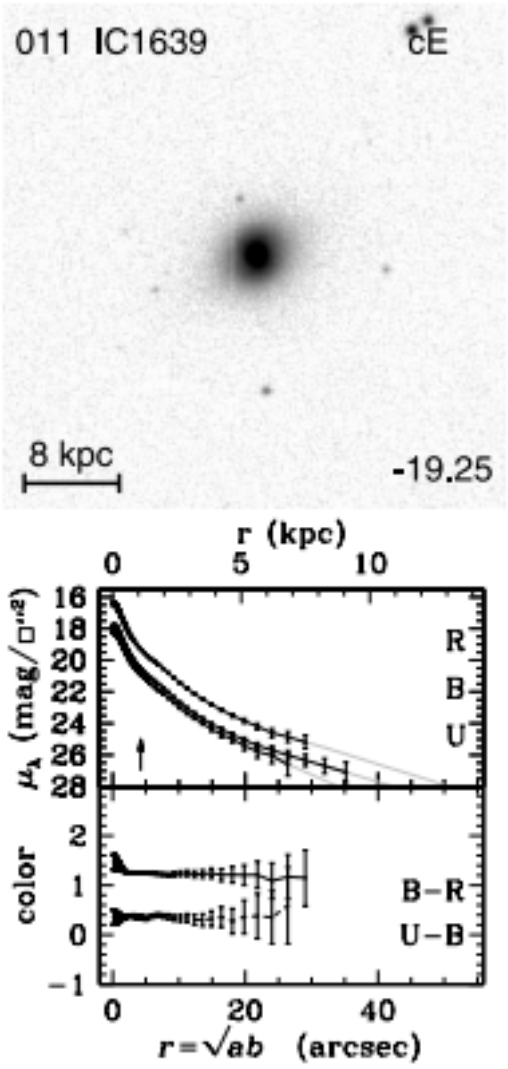

Fig. 10.— The R band image and the radial profiles of UGC 439. The top panel shows the radial dependence of the surface brightness in U, B and R and the bottom panel shows the radial dependence of the corresponding colors (Jansen et al. 2000a).

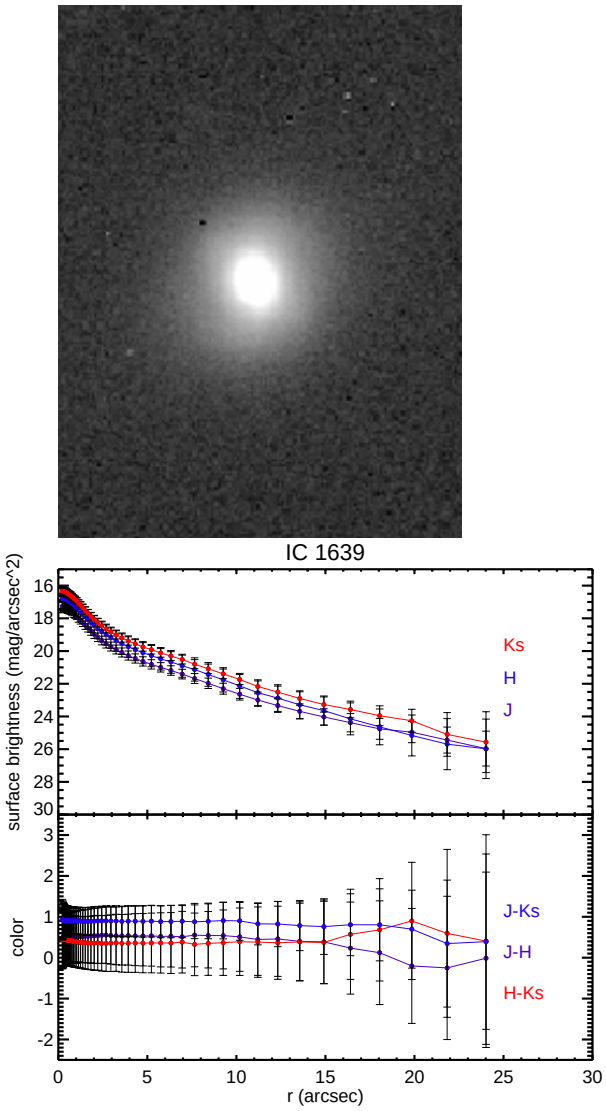

Fig. 11.— The J band image and the J, H and K_s radial profiles of UGC 439. The top panel shows the radial dependence of the surface brightness inJ, H and $K_s$and the bottom panel shows the radial dependence of the corresponding colors. The image was obtained by Loeffler.

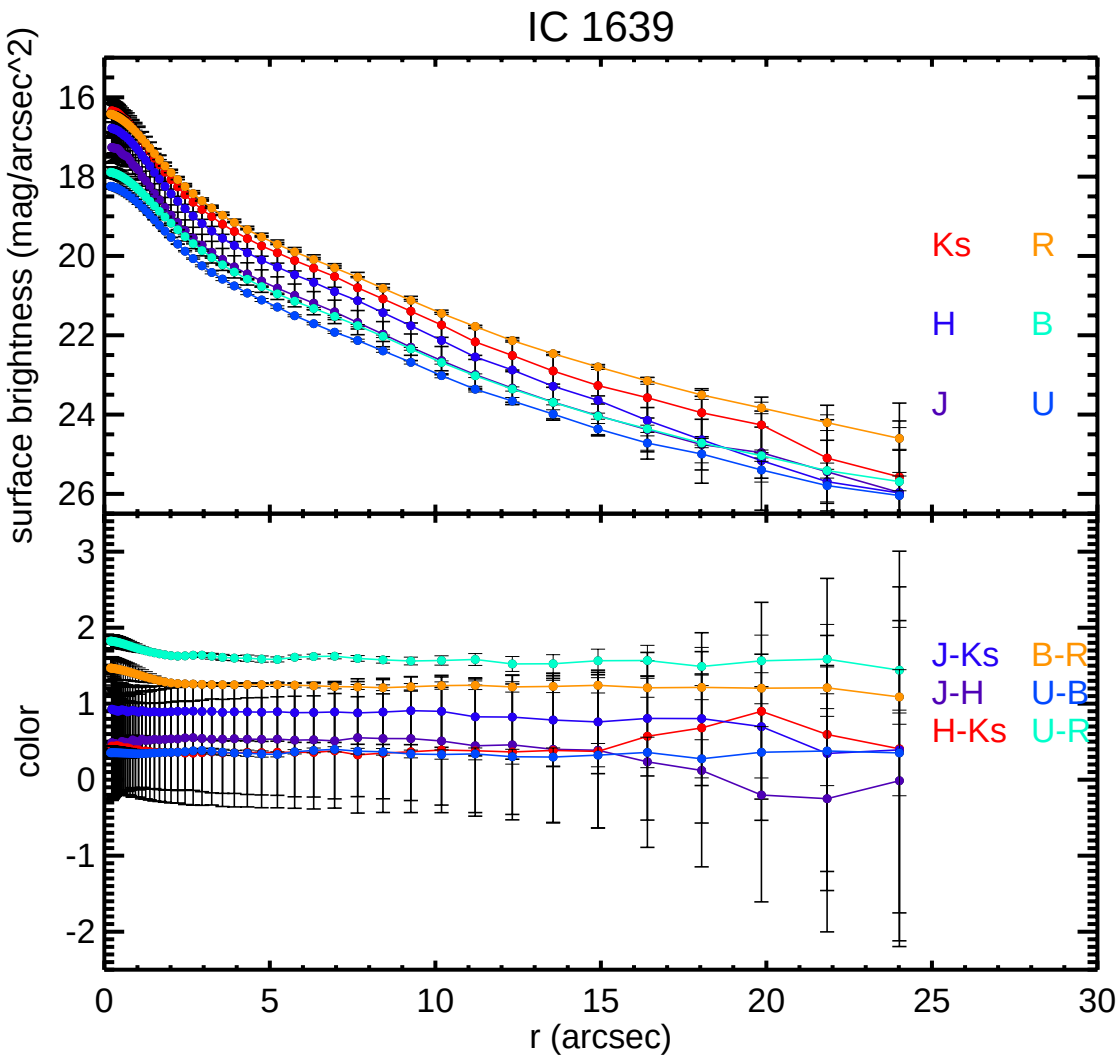

Fig. 12.— The radial dependence of the surface brightness in J, H and K_s along with those in U, B and R surface brightness from Jansen et al. (2000a)(top panel) and corresponding colors (bottom panel) are presented for IC 1639.

6. Conclusions

We successfully developed a pipeline to process PISCES infrared images and an IDL code to reduce and perform aperture photometry on galaxies with zero ellipticity such as UGC 439. The PISCES J, H and K_s band images are deeper than the 2MASS images of UGC 439 enabling us to studying the outer regions of the galaxy. The color radial profile that we present show that UGC 439 has a flat color profile in the infrared.

A. Derivation of Calibration Equations 6 and 7

We present the algebra to find the solutions for the surface brightnesses and the random errors associated with each solution. Equation A1 summarizes the calibration equations for J, H and K_s intensity profiles:

$$\begin{cases} \mu_J(r) = \mu_{J,i}(r) - Z_J - \epsilon_J X - c_J(\mu_J - \mu_{K_s})(r), \\ \mu_H(r) = \mu_{H,i}(r) - Z_H - \epsilon_H X - c_H(\mu_H - \mu_{K_s})(r), \\ \mu_{K_s}(r) = \mu_{K_s,i}(r) - Z_{K_s} - \epsilon_{K_s} X - c_{K_s}(\mu_J - \mu_{K_s})(r). \end{cases} \tag{A1}$$

In order to solve for the each surface brightnesses solution, we define

$$\begin{cases} P_J(r) = \mu_{J,i}(r) - Z_J - \epsilon_J X, \\ P_H(r) = \mu_{H,i}(r) - Z_H - \epsilon_H X, \\ P_{K_s}(r) = \mu_{K_s,i}(r) - Z_{K_s} - \epsilon_{K_s} X. \end{cases} \tag{A2}$$

By substituting Equations A2 into Equations A1, we can rewrite Equations A1 as:

$$(1 + c_J)\mu_J(r) = P_J(r) + c_J\mu_{K_s}(r), \tag{A3}$$

$$(1 + c_H)\mu_H(r) = P_H(r) + c_H\mu_{K_s}(r), \tag{A4}$$

$$(1 - c_{K_s})\mu_{K_s}(r) = P_{K_s}(r) - c_{K_s}\mu_J(r). \tag{A5}$$

We first find the solution for the surface brightness of J by substituting Equation A5 into Equation A3:

$$(1 + c_J)\mu_J(r) = P_J(r) + c_J\left(\frac{P_{K_s}(r) - c_{K_s}\mu_J(r)}{1 - c_{K_s}}\right). \tag{A6}$$

Multiplying both sides by $1 - c_{K_s}$ yields:

$$(1 + c_J)(1 - c_{K_s})\mu_J(r) = P_J(r)(1 - c_{K_s}) + c_J P_{K_s}(r) - c_J c_{K_s}\mu_J(r). \quad \text{(A7)}$$

Adding $c_J c_{K_s}\mu_J(r)$ to both sides and expanding the left side yields:

$$(1 + c_J - c_{K_s} - c_J c_{K_s})\mu_J(r) + c_J c_{K_s}\mu_J(r) = P_J((r)1 - c_{K_s}) + c_J P_{K_s}(r). \quad \text{(A8)}$$

By factoring $\mu_J(r)$, we can rewrite Equation A8 as

$$(1 + c_J - c_{K_s} - c_J c_{K_s} + c_J c_{K_s})\mu_J(r) = P_J(r)(1 - c_{K_s}) + c_J P_{K_s}(r). \quad \text{(A9)}$$

The solution for the surface brightness of J is

$$\mu_J(r) = \frac{P_J(r)(1 - c_{K_s}) + c_J P_{K_s}(r)}{1 + c_J - c_{K_s}}. \quad \text{(A10)}$$

We can find the solution for the surface brightness of K_s by substituting Equation A3 into Equation A5 and following the method described above:

$$(1 - c_{K_s})\mu_{K_s}(r) = P_{K_s}(r) - c_{K_s}\left(\frac{P_J(r) + c_J\mu_{K_s}(r)}{1 + c_J}\right), \quad \text{(A11)}$$

$$(1 + c_J)(1 - c_{K_s})\mu_{K_s}(r) = P_{K_s}(r)(1 + c_J) - c_{K_s}P_J(r) - c_{K_s}c_J\mu_{K_s}(r), \quad \text{(A12)}$$

$$(1 + c_J - c_{K_s} - c_J c_{K_s})\mu_{K_s}(r) + c_{K_s}c_J\mu_{K_s}(r) = P_{K_s}(r)(1 + c_J) - c_{K_s}P_J(r), \quad \text{(A13)}$$

$$(1 + c_J - c_{K_s} - c_J c_{K_s} + c_J c_{K_s})\mu_{K_s}(r) = P_{K_s}(r)(1 + c_J) - c_{K_s}P_J(r), \quad \text{(A14)}$$

$$\mu_{K_s}(r) = \frac{P_{K_s}(r)(1 + c_J) - c_{K_s}P_J(r)}{1 + c_J - c_{K_s}}. \quad \text{(A15)}$$

In order to solve for the surface brightness of H, we substitute Equation A15 into Equation 4:

$$(1+c_H)\mu_H(r) = P_H(r) + c_H\left(\frac{P_{K_s}(r)(1+c_J) - c_{K_s}P_J(r)}{1+c_J-c_{K_s}}\right). \tag{A16}$$

Then by following similar algebraic steps, the surface brightness of H is:

$$(1+c_H)\mu_H(r) = \frac{P_H(r)(1+c_J-c_{K_s}) + c_H(P_{K_s}(r)(1+c_J) - c_{K_s}P_J(r))}{1+c_J-c_{K_s}}, \tag{A17}$$

$$\begin{aligned}&(1+c_H)(1+c_J-c_{K_s})\mu_H(r) = \\ &\quad P_H(r)(1+c_J-c_{K_s}) + c_H(P_{K_s}(r)(1+c_J) - c_{K_s}P_J(r)),\end{aligned} \tag{A18}$$

$$\begin{aligned}&(1+c_J+c_H-c_{K_s}+c_Jc_H-c_Hc_{K_s})\mu_H(r) = \\ &\quad P_H(r)(1+c_J-c_{K_s}) + c_H(P_{K_s}(r)(1+c_J) - c_{K_s}P_J(r)),\end{aligned} \tag{A19}$$

$$\mu_H(r) = \frac{P_H(r)(1+c_J-c_{K_s}) + c_H(P_{K_s}(r)(1+c_J) - c_{K_s}P_J(r))}{1+c_J+c_H-c_{K_s}+c_Jc_H-c_Hc_{K_s}}. \tag{A20}$$

In order to find the random error in the surface brightness of J, we solved the following equation:

$$\begin{aligned}\sigma_{\mu_J}(r) = &\sqrt{\left(\frac{\partial\mu_J(r)}{\partial P_J(r)}\right)^2\sigma^2_{P_J(r)} + \left(\frac{\partial\mu_J(r)}{\partial P_{K_s}(r)}\right)^2\sigma^2_{P_{K_s}(r)} + \left(\frac{\partial\mu_J(r)}{\partial c_{K_s}}\right)^2\sigma^2_{c_{K_s}}} \\ &\overline{+\left(\frac{\partial\mu_J(r)}{\partial c_J}\right)^2\sigma^2_{c_J}}.\end{aligned} \tag{A21}$$

By algebra, Equation A21 yields.

$$\sigma_{\mu_J}(r) = \sqrt{\left(\frac{1-c_{K_s}}{1+c_J-c_{K_s}}\right)^2 \sigma^2_{P_J(r)} + \left(\frac{c_J}{1+c_J-c_{K_s}}\right)^2 \sigma^2_{P_{K_s}(r)} + \left(\frac{-P_J(r)(1+c_J-c_{K_s}) + (P_J(r)(1-c_{K_s}) + c_J P_{K_s}(r))}{(1+c_J-c_{K_s})^2}\right)^2 \sigma^2_{c_{K_s}} + \left(\frac{P_{K_s}(r)(1+c_J-c_{K_s}) + (P_J(r)(1-c_{K_s}) + c_J P_{K_s}(r))}{(1+c_J-c_{K_s})^2}\right)^2 \sigma^2_{c_J}}. \tag{A22}$$

By substituting Equation A3 into the 3^{rd} and 4^{th} term, we can rewrite Equation A22 as;

$$\sigma_{\mu_J}(r) = \sqrt{\left(\frac{1-c_{K_s}}{1+c_J-c_{K_s}}\right)^2 \sigma^2_{P_J(r)} + \left(\frac{c_J}{1+c_J-c_{K_s}}\right)^2 \sigma^2_{P_{K_s}(r)} + \left(\frac{-P_J(r)(1+c_J-c_{K_s}) + \mu_J(r)(1+c_J-c_{K_s})}{(1+c_J-c_{K_s})^2}\right)^2 \sigma^2_{c_{K_s}} + \left(\frac{P_{K_s}(r)(1+c_J-c_{K_s}) + \mu_J(r)(1+c_J-c_{K_s})}{(1+c_J-c_{K_s})^2}\right)^2 \sigma^2_{c_J}}. \tag{A23}$$

Simplifying the 3^{rd} and 4^{th} term of Equation A23 yields:

$$\sigma_{\mu_J}(r) = \sqrt{\left(\frac{1-c_{K_s}}{1+c_J-c_{K_s}}\right)^2 \sigma^2_{P_J(r)} + \left(\frac{c_J}{1+c_J-c_{K_s}}\right)^2 \sigma^2_{P_{K_s}(r)} + \left(\frac{-P_J(r)+\mu_J(r)}{1+c_J-c_{K_s}}\right)^2 \sigma^2_{c_{K_s}} + \left(\frac{P_{K_s}(r)+\mu_J(r)}{1+c_J-c_{K_s}}\right)^2 \sigma^2_{c_J}}. \tag{A24}$$

By factoring the denominator out and expanding the 3^{rd} and 4^{th} term yields:

$$\sigma_{\mu_J}(r) = \sqrt{\left(\frac{1}{1+c_J-c_{K_s}}\right)^2} \sqrt{(1-c_{K_s})^2\sigma^2_{P_J(r)} + c_J^2\sigma^2_{P_{K_s}(r)} + [P_J^2(r) + 2\mu_J(r)P_J + \mu_J^2(r)]\sigma^2_{c_{K_s}} + [P^2_{K_s}(r) + 2\mu_J(r)P_{K_s} + \mu_J^2(r)]\sigma^2_{c_J}}. \tag{A25}$$

By assuming the individual errors in the color terms are Gaussian in nature and uncorrelated the random error in the surface brightness of J is

$$\sigma_{\mu_J}(r) = \frac{1}{1+c_J-c_{K_s}}\sqrt{(1-c_{K_s})^2\sigma^2_{P_J(r)} + c_J^2\sigma^2_{P_{K_s}(r)} + [P_J^2(r)+\mu_J^2(r)]\sigma^2_{c_{K_s}}} \\ \overline{+[P^2_{K_s}(r)+\mu_J^2(r)]\sigma^2_{c_J}}. \tag{A26}$$

By following the same algebraic steps, the random error in the surface brightness of K_s is:

$$\sigma_{\mu_{K_s}}(r) = \sqrt{\left(\frac{\partial\mu_{K_s}(r)}{\partial P_{K_s}(r)}\right)^2\sigma^2_{P_{K_s}(r)} + \left(\frac{\partial\mu_{K_s}(r)}{\partial P_J(r)}\right)^2\sigma^2_{P_J(r)} + \left(\frac{\partial\mu_{K_s}(r)}{\partial c_{K_s}}\right)^2\sigma^2_{c_{K_s}}} \\ \overline{+\left(\frac{\partial\mu_{K_s}(r)}{\partial c_J}\right)^2\sigma^2_{c_J}}, \tag{A27}$$

$$\sigma_{\mu_{K_s}}(r) = \sqrt{\left(\frac{1+c_J}{1+c_J-c_{K_s}}\right)^2\sigma^2_{P_{K_s}(r)} + \left(\frac{-c_{K_s}}{1+c_J-c_{K_s}}\right)^2\sigma^2_{P_J(r)}} \\ \overline{+\left(\frac{-P_J(r)(1+c_J-c_{K_s}) + (P_{K_s}(r)(1+c_J) - c_{K_s}P_J(r))}{(1+c_J-c_{K_s})^2}\right)^2\sigma^2_{c_{K_s}}} \\ \overline{+\left(\frac{P_{K_s}(r)(1+c_J-c_{K_s}) - (P_{K_s}(r)(1+c_J) - c_{K_s}P_J(r))}{(1+c_J-c_{K_s})^2}\right)^2\sigma^2_{c_J}}. \tag{A28}$$

By substituting Equation A5 into the 3^{rd} and 4^{th} term, we can rewrite Equation A28 as;

$$\sigma_{\mu_{K_s}}(r) = \sqrt{\left(\frac{1+c_J}{1+c_J-c_{K_s}}\right)^2\sigma^2_{P_{K_s}(r)} + \left(\frac{-c_{K_s}}{1+c_J-c_{K_s}}\right)^2\sigma^2_{P_J(r)}} \\ \overline{+\left(\frac{-P_J(r)(1+c_J-c_{K_s}) + \mu_{K_s}(r)(1+c_J-c_{K_s})}{(1+c_J-c_{K_s})^2}\right)^2\sigma^2_{c_{K_s}}} \\ \overline{+\left(\frac{P_{K_s}(r)(1+c_J-c_{K_s}) + \mu_{K_s}(r)(1+c_J-c_{K_s})}{(1+c_J-c_{K_s})^2}\right)^2\sigma^2_{c_J}}, \tag{A29}$$

$$\sigma_{\mu_{K_s}}(r) = \sqrt{\left(\frac{1+c_J}{1+c_J-c_{K_s}}\right)^2 \sigma^2_{P_{K_s}(r)} + \left(\frac{-c_{K_s}}{1+c_J-c_{K_s}}\right)^2 \sigma^2_{P_J(r)} + \left(\frac{-P_J(r)+\mu_{K_s}(r)}{1+c_J-c_{K_s}}\right)^2 \sigma^2_{c_{K_s}} + \left(\frac{P_{K_s}(r)+\mu_{K_s}(r)}{1+c_J-c_{K_s}}\right)^2 \sigma^2_{c_J}}, \tag{A30}$$

$$\sigma_{\mu_{K_s}}(r) = \sqrt{\left(\frac{1}{1+c_J-c_{K_s}}\right)^2} \sqrt{(1+c_J)^2\sigma^2_{P_{K_s}(r)} + c^2_{K_s}\sigma^2_{P_J(r)} + [P^2_J(r) + 2P_J(r)\mu_{K_s}(r) + \mu^2_{K_s}(r)]\sigma^2_{c_{K_s}} + [P^2_{K_s}(r) + 2P_{K_s}(r)\mu_{K_s}(r) + \mu^2_{K_s}(r)]\sigma^2_{c_J}}. \tag{A31}$$

By assuming the individual errors in the color terms are Gaussian in nature and uncorrelated the random error in the surface brightness of K_s is:

$$\sigma_{\mu_{K_s}}(r) = \frac{1}{1+c_J-c_{K_s}} \sqrt{(1+c_J)^2\sigma^2_{P_{K_s}(r)} + c^2_{K_s}\sigma^2_{P_J(r)} + [P^2_J(r) + \mu^2_{K_s}(r)]\sigma^2_{c_{K_s}} + [P^2_{K_s}(r) + \mu^2_{K_s}(r)]\sigma^2_{c_J}}. \tag{A32}$$

In order to find the random error in the surface brightness of H, we solved the following equation:

$$\sigma_{\mu_H}(r) = \sqrt{\left(\frac{\partial\mu_H(r)}{\partial P_J(r)}\right)^2 \sigma^2_{P_J(r)} + \left(\frac{\partial\mu_H(r)}{\partial P_{K_s}(r)}\right)^2 \sigma^2_{P_{K_s}(r)} + \left(\frac{\partial\mu_H(r)}{\partial P_H(r)}\right)^2 \sigma^2_{P_H(r)} + \left(\frac{\partial\mu_H(r)}{\partial c_{K_s}}\right)^2 \sigma^2_{c_{K_s}} + \left(\frac{\partial\mu_H(r)}{\partial c_J}\right)^2 \sigma^2_{c_J} + \left(\frac{\partial\mu_H(r)}{\partial c_H}\right)^2 \sigma^2_{c_H}}} \tag{A33}$$

By taking the partial derivative of Equation A20 and defining ϵ as $1 + c_J + c_H -$

$c_{K_s} + c_J c_H - c_H c_{K_s}$ and nm as $(1 + c_J - c_{K_s} E$, we can rewrite Equation A33 as:

$$\sigma_{\mu_H}(r) = \sqrt{\left(\frac{-c_H c_{K_s}}{\epsilon}\right)^2 \sigma^2_{P_J(r)} + \left(\frac{c_H(1+c_J)}{\epsilon}\right)^2 \sigma^2_{P_{K_s}(r)} + \left(\frac{1+c_J-c_{K_s}}{\epsilon}\right)^2 \sigma^2_{P_H(r)} + \left(\frac{(-P_H(r) - c_H P_J(r))\epsilon + (P_H(r)nm + c_H(P_{K_s}(r)(1+c_J)))(1+c_H)}{\epsilon^2}\right)^2 \sigma^2_{c_{K_s}} + \left(\frac{(P_H(r) + c_H P_{K_s}(r))\epsilon - (P_H(r)nm + c_H(P_{K_s}(r)(nmP_J(r)))(1+c_H)}{\epsilon^2}\right)^2 \sigma^2_{c_J} + \left(\frac{P_{K_s}(r)nmP_J(r)\epsilon - (P_H(r)nm + c_H(P_{K_s}(r)(1+c_J) - c_{K_s}P_J(r)))nm}{\epsilon^2}\right)^2 \sigma^2_{c_H}}. \tag{A34}$$

Substituting Equation A4 into the 3^{rd} and 4^{th} term, Equation A34 can be rewritten as

$$\sigma_{\mu_H}(r) = \sqrt{\left(\frac{-c_H c_{K_s}}{\epsilon}\right)^2 \sigma^2_{P_J(r)} + \left(\frac{c_H(1+c_J)}{\epsilon}\right)^2 \sigma^2_{P_{K_s}(r)} + \left(\frac{1+c_J-c_{K_s}}{\epsilon}\right)^2 \sigma^2_{P_H(r)} + \left(\frac{(-P_H(r) - c_H P_J(r))\epsilon + \mu_H(r)\epsilon(1+c_H)}{\epsilon^2}\right)^2 \sigma^2_{c_{K_s}} + \left(\frac{(P_H(r) + c_H P_{K_s}(r))\epsilon - \mu_H(r)\epsilon(1+c_H)}{\epsilon^2}\right)^2 \sigma^2_{c_J} + \left(\frac{(P_{K_s}(r)nmP_J(r))\epsilon - \mu_H(r)\epsilon nm}{\epsilon^2}\right)^2 \sigma^2_{c_H}}. \tag{A35}$$

By simplifying, substituting ϵ and nm and expanding the 3^{rd} and 4^{th} term yields:

$$\begin{aligned}\sigma_{\mu_H}(r) =&\sqrt{\left(\frac{-c_H c_{K_s}}{1+c_J+c_H-c_{K_s}+c_J c_H-c_H c_{K_s}}\right)^2\sigma^2_{P_J(r)}}\\
&\overline{+\left(\frac{c_H(1+c_J)}{1+c_J+c_H-c_{K_s}+c_J c_H-c_H c_{K_s}}\right)^2\sigma^2_{P_{K_s}(r)}}\\
&\overline{+\left(\frac{1+c_J-c_{K_s}}{1+c_J+c_H-c_{K_s}+c_J c_H-c_H c_{K_s}}\right)^2\sigma^2_{P_H(r)}}\\
&\overline{+\left(\frac{-P_H(r)-c_H P_J(r)+\mu_H(r)c_H+\mu_H(r)}{(1+c_J+c_H-c_{K_s}+c_J c_H-c_H c_{K_s})}\right)^2\sigma^2_{c_{K_s}}}\\
&\overline{+\left(\frac{P_H(r)+c_H P_{K_s}(r)-\mu_H(r)c_H-\mu_H(r)}{1+c_J+c_H-c_{K_s}+c_J c_H-c_H c_{K_s}}\right)^2\sigma^2_{c_J}}\\
&\overline{+\left(\frac{P_{K_s}(r)+P_{K_s}c_J-c_{K_s}P_J(r)-\mu_H(r)c_J+\mu_H(r)c_{K_s}-\mu_H(r)}{1+c_J+c_H-c_{K_s}+c_J c_H-c_H c_{K_s}}\right)^2\sigma^2_{c_H}}.\end{aligned} \tag{A36}$$

By assuming the individual errors in the color terms are Gaussian in nature and uncorrelated the random error in the surface brightness of H is:

$$\begin{aligned}\sigma_{\mu_H}(r) = \sqrt{\frac{1}{1+c_J+c_H-c_{K_s}+c_J c_H-c_H c_{K_s}}}&\sqrt{c_H^2 c_{K_s}^2\sigma^2_{P_J(r)}+(c_H(1+c_J))^2\sigma^2_{P_{K_s}(r)}}\\
&\overline{+(1+c_J-c_{K_s})^2\sigma^2_{P_H(r)}}\\
&\overline{+[P_H^2(r)+\mu_H^2(r)]\sigma^2_{c_{K_s}}}\\
&\overline{+[P_H^2(r)+\mu_H^2(r)]\sigma^2_{c_J}}\\
&\overline{+[P_{K_s}^2(r)+\mu_H^2(r)]\sigma^2_{c_H}},\end{aligned} \tag{A37}$$

$$\sigma_{\mu_H}(r) = \frac{1}{(1+c_J-c_{K_s})(1+c_H)}\sqrt{c_H^2 c_{K_s}^2 \sigma_{P_J(r)}^2 + (c_H(1+c_J))^2 \sigma_{P_{K_s}(r)}^2}$$
$$\overline{+(1+c_J-c_{K_s})^2 \sigma_{P_H(r)}^2 + [P_H^2(r)+\mu_H^2(r)]\sigma_{c_{K_s}}^2}$$
$$\overline{+[P_H^2(r)+\mu_H^2(r)]\sigma_{c_J}^2 + [P_{K_s}^2(r)+\mu_H^2(r)]\sigma_{c_H}^2}. \quad \text{(A38)}$$

B. Alternative Calibration Method

We also tried to determine the photometric calibration of the images of UGC 439 by measuring the instrumental magnitudes of multiple 2MASS AAA stars in the field of the image. Table 4 presents a list of the 2MASS stars. Column (1) lists the name and Columns (2-7) list the 2MASS and instrumental magnitudes for J, H and K_s bands. Fig.13 is the J-band stacked images of UGC 349 with the 2MASS stars indicated by blue circles.

Since the 2MASS stars are in the same field of view of the images and were taken at the same airmass, we do not fit for the extinction value and therefore the

Table 4. PHOTOMETRIC CONSTANTS

Star	J (2MASS)[a] (mag)	J_i (mag)	H (2MASS)[a] (mag)	H_I (mag)	K_s (2MASS)[a] (mag)	$K_{s,i}$ (mag)
1	12.49±0.02	-6.10±0.03	12.02±0.05	-6.38±0.02	11.97±0.07	-6.09±0.02
2	15.51±0.06	-5.69±0.05	15.14±0.06	-6.05±0.06	14.91±0.08	-5.82±0.06
3	15.04±0.04	-6.25±0.03	14.30±0.05	-6.38±0.04	14.14±0.08	-6.08±0.04
4	14.80±0.04	-5.16±0.05	14.30±0.09	-5.29±0.04	14.04±0.09	-5.09±0.04

[a]Retrieved from Smithsonian Institution.

fit applied to extract the photometric calibrations are

$$\begin{cases} J - J_i = -Z_J - c_J(J - K_s), \\ H - H_i = -Z_H - c_H(H - K_s), \\ K_s - K_{s,i} = -Z_{K_s} - c_{K_s}(J - K_s). \end{cases} \tag{B1}$$

Fig.14 shows the fit for all three bands. From the slope and the y-intercept of each fit, the color term and the zero point can be extracted for the respected filters. The correlation coefficient from these particular fits are 0.643, 0.679 and 0.448 for the J, H and K_s bands respectively. Thus, we determined the photometric calibrations extracted using the Persson standard stars are more trustworthy than the values extracted from the 2MASS stars.

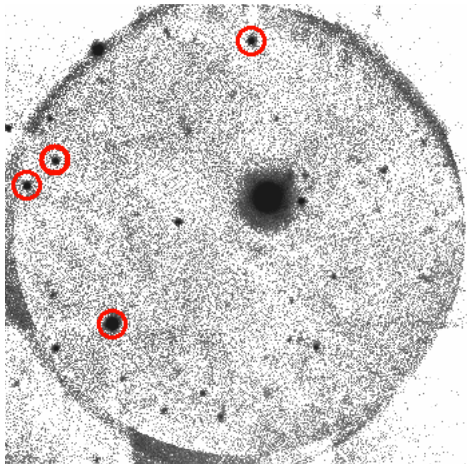

Fig. 13.— The J-band stacked image of UGC 349. The AAA 2MASS stars are enclosed in blue circles.

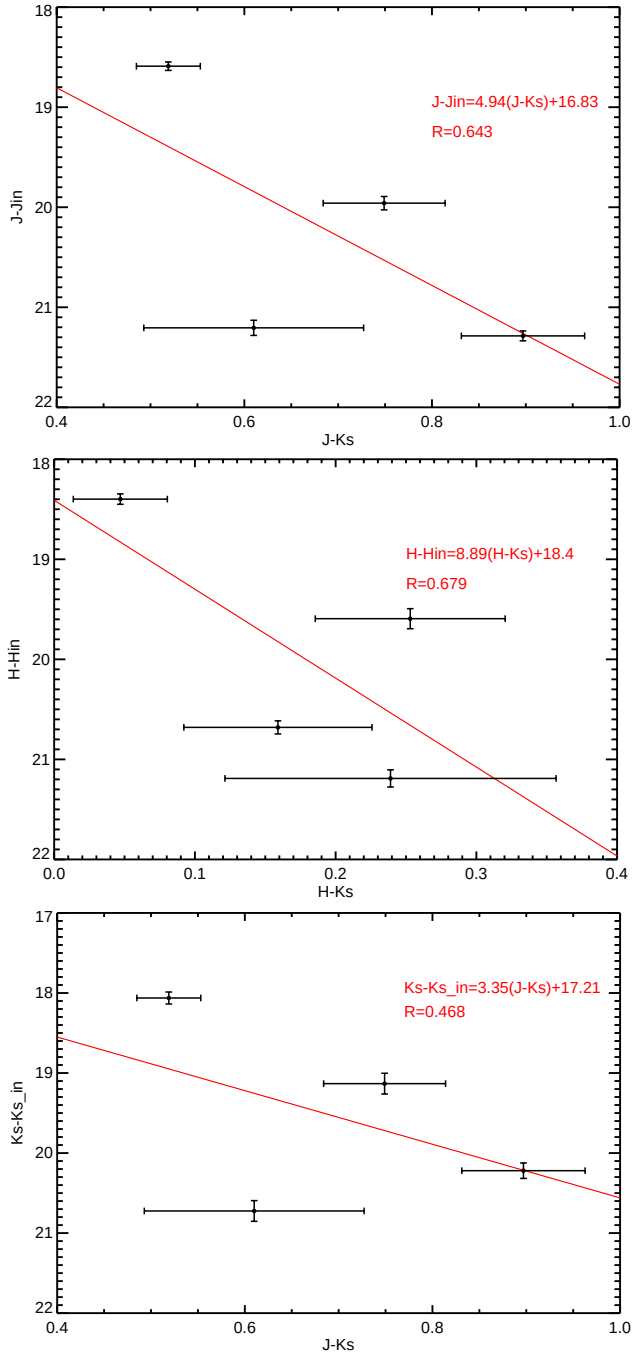

Fig. 14.— The difference between the 2mass magnitude and instrumental magnitude versus a 2mass color. From top to bottom: J-Jin vs. J-Ks, H-Hin vs. H-Ks, and Ks-Ks_in vs J-Ks.

REFERENCES

Binggeli, B., Sandage, A., & Tammann, G. A. 1985, AJ, 90, 1681

Beckwith, S. V., Somerville, R. S., Ferguson, H. C., Caldwell, J. A., Koekemoer, A. M., Stiavelli, M., et al. 2006, AJ, 132, 1729

Carroll, B. W., & Ostlie, D. A. 1996, *Galaxies and the Universe . An introduction to modern astrophysics* (1st ed.; San Francisco: Pearson Addison-Wesley), 987-1073

Fabricant, D., Cheimets, P., Caldwell, N., & Geary, J. 1998, PASP, 110, 79

Franx, M., Illingworth, B., & Heckman, T. 1989, AJ, 89, 538

The Hubble Tuning Fork. (n.d.). *SDSS SkyServer DR7*. Retrieved October 1, 2013, from http://cas.sdss.org/

Guerra, C. J., Boutsia, K., Rakich, A., Green, R., McCarthy D., & Kulesa C. 2013, PISCES Infrared Imager Performance with the Large Binocular Telescope Adaptive Optics System. Retrieved 2014, from http://www.lbto.org/

Huchra, J., Davis, M., Latham, D., & Tonry, J. 1983, ApJS, 52, 89

Jansen R. A. 2000, *The nearby field galaxy survey : a spectrophotometric study of 196 galaxies in the local field.* University of Groningev, PhD Thesis

Jansen, R.A.,Franx, M., Fabricant, D., & Caldwell, N. 2000a, ApJS, 126, 271

Jansen, R.A., Fabricant, D., Franx, M., & Caldwell, N. 2000b, ApJS, 126,331

Jansen, R.A.,Franx, M., Fabricant, D., & Caldwell, N. 2001, ApJ, 551, 825

Kaleida, C., Jansen, R., McCarthy, D., & Kulesa, C. 2010, Observing Request.

Kannappan, S.J, & Fabricant, D. 2001, AJ, 121, 140

Kannappan, S.J., Fabricant, D., & Franx, M. 2002, AJ, 123, 2358

Kannappan, S.J., & Barton, E.J. 2004, AJ, 127, 2694

Karachentsev, I. D., & Macharov, D. A. 1996, AJ, 111,794

Kewley, L.J., Geller, M.J., Jansen, R.A., & Dopita, M.A. 2002, AJ, 124, 3135

Kewley, L.J., Geller, M.J., & Jansen, R.A. 2004, AJ, 127, 2002

Kewley, L.J., Jansen, R.A., & Geller, M.J. 2005, PASP, 117, 227

Kirby, E.M., Jerjen, H., Ryder, S.D., & Driver, S. P. 2008, AJ, 136, 1866

Marzke, R.O., Huchra, J.P., & Geller, M. J. 1994, ApJ, 428, 43

McCarthy et al. 2001, PASP, 113, 353

Peletier, R.F., Davies, R.L., Illingworth, G.D., Davis, L.E., & Cawson, M. 1990, AJ, 100, 1091

Persson, S.E., Murphy, D.C., Krzeminski, W., Roth, M., & Rieke, M.J. 1998, AJ, 116, 5

Schlafly, E. F., & Finkbeiner, D. P. 2011, ApJ, 737, 103

Sparke, L. S., & Gallagher, J. S. 2000, *Galaxies in the universe: an introduction.* (2nd ed.; New York: Cambridge University Press)

Tamura, N., & Ohta, K. 2003, AJ, 126, 596

Taylor, V.A., Jansen R.A., Windhorst, R.A., Odewahn, S.C., & Hibbard, J.E. 2005, ApJ, 630, 784

Vader, J.P., Vigroux, L., Lachieze-Rey, M., & Souviron, J. 1988, A&A, 203, 217

Williams, R.E., et al. 1996, AJ, 112, 1335

von Braun, K., Chiboucas, K., Minske, J. K., Salgado, J.K., & Worthey, G. 1998, PASP, 110, 810

Yahil, A., Tammann, G. A., & Sandage, A. 1977, ApJ, 217 903

This manuscript was prepared with the AAS LaTeX macros v5.2.